ALMA chemical survey of disk-outflow sources in Taurus (ALMA-DOT): IV. Thioformaldehyde (H2CS) in protoplanetary discs: Spatial distributions and binding energies

(Article begins on next page)

14 December 2021

ALMA chemical survey of disk-outflow sources in Taurus (ALMA-DOT)

IV. Thioformaldehyde (H₂CS) in protoplanetary disks: spatial distributions and binding energies

C. Codella[1,2], L. Podio[1], A. Garufi[1], J. Perrero[3], P. Ugliengo[3], D. Fedele[1,4], C. Favre[2], E. Bianchi[2], C. Ceccarelli[2], S. Mercimek[1,5], F. Bacciotti[1], K.L.J. Rygl[6], and L. Testi[7,8,1]

[1] INAF, Osservatorio Astrofisico di Arcetri, Largo E. Fermi 5, 50125 Firenze, Italy
[2] Univ. Grenoble Alpes, CNRS, Institut de Planétologie et d'Astrophysique de Grenoble (IPAG), 38000 Grenoble, France
[3] Dipartimento di Chimica and Nanostructured Interfaces and Surfaces (NIS) Centre, Università degli Studi di Torino, via P. Giuria 7, 10125 Torino, Italy
[4] INAF, Osservatorio Astrofisico di Torino, Via Osservatorio 20, I-10025 Pino Torinese, Italy
[5] Università degli Studi di Firenze, Dipartimento di Fisica e Astronomia, Via G. Sansone 1, 50019 Sesto Fiorentino, Italy
[6] INAF, Istituto di Radioastronomia & Italian ALMA Regional Centre, via P. Gobetti 101, 40129 Bologna, Italy
[7] European Southern Observatory, Karl-Schwarzschild-Strasse 2, 85748 Garching bei München, Germany
[8] Excellence Cluster Origins, Boltzmannstrasse 2, 85748 Garching bei München, Germany

Received date; accepted date

ABSTRACT

Context. Planet formation starts around Sun-like protostars with ages ≤ 1 Myr: what is the chemical compositions in disks?
Aims. To trace the radial and vertical spatial distribution of H₂CS, a key species of the S-bearing chemistry, in protoplanetary disks. To analyse the observed distributions in light of the H₂CS binding energy, in order to discuss the role of thermal desorption in enriching the gas disk component.
Methods. In the context of the ALMA chemical survey of Disk-Outflow sources in the Taurus star forming region (ALMA-DOT), we observed five Class I or early Class II sources with the o–H₂CS($7_{1,6} - 6_{1,5}$) line. ALMA-Band 6 was used, reaching spatial resolutions ≃ 40 au, i.e. Solar System spatial scales. We also estimated the binding energy of H₂CS using quantum mechanical calculations, for the first time, for an extended, periodic, crystalline ice.
Results. We imaged H₂CS emission in two rotating molecular rings in the HL Tau and IRAS04302+2247 disks. The outer radii are ~ 140 au (HL Tau), and 115 au (IRAS 04302+2247). The edge-on geometry of IRAS 04302+2247 allows us to reveal that H₂CS emission peaks, at radii of 60–115 au, at $z = \pm 50$ au from the equatorial plane. Assuming LTE conditions, the column densities are ~ 10^{14} cm^{-2}. Upper limits of a few 10^{13} cm^{-2} have been estimated for the H₂CS column densities in DG Tau, DG Tau B, and Haro 6-13 disks. For HL Tau, we derive, for the first time, the [H₂CS]/[H] abundance in a protoplanetary disk ($\simeq 10^{-14}$). The binding energy of H₂CS computed for extended crystalline ice and amorphous ices is 4258 K and 3000-4600 K, respectively, implying a thermal evaporation where dust temperature is ≥ 50–80 K.
Conclusions. H₂CS traces the so-called warm molecular layer, a region previously sampled using CS, and H₂CO. Thioformaldehyde peaks closer to the protostar than H₂CO and CS, plausibly due to the relatively high-excitation level of observed $7_{1,6} - 6_{1,5}$ line (60 K). The H₂CS binding energy implies that thermal desorption dominates in thin, au-sized, inner and/or upper disk layers, indicating that the observed H₂CS emitting up to radii larger than 100 au is likely injected in the gas due to non-thermal processes.

Key words. astrochemistry - protoplanetary disks - methods: numerical - ISM: molecules - ISM: individual objects: HL TAU, IRAS04302+2247

1. Introduction

Low-mass star formation is the process starting from a molecular cloud and ending with a Sun-like star with its own planetary system. According to the classical scenario (e.g. Andre et al. 2000; Caselli & Ceccarelli 2012, and references therein), the central object increases its mass through an accretion disk, while a fast jet contributes in removing the angular momentum excess. While the star accrete its mass, part of the material in the disk is incorporated to form planets. As the physical process proceeds, also

the chemistry evolves towards a complex gas composition (see Ceccarelli et al. 2007; Herbst & van Dishoeck 2009). Several observational programs have been dedicated to the chemical content of *protostellar* envelopes/disks using both single-dishes and interferometers at mm-wavelenghts (IRAM 30-m ASAI (Lefloch et al. 2018); ALMA PILS (Jørgensen et al. 2016); IRAM PdBI CALYPSO (Belloche et al. 2020); IRAM NOEMA SOLIS (Ceccarelli et al. 2017); ALMA FAUST[1], Bianchi et al. 2020). Nevertheless, the chemical content of the *protoplanetary* disks is still poorly known. Tiny outer molecular layers (and thus small column densities) are formed due to thermal or UV-photo/CR-

---

[1] http://faust-alma.riken.jp

induced desorption (e.g., Semenov & Wiebe 2011; Walsh et al. 2014, 2016; Loomis et al. 2015; Le Gal et al. 2019). More precisely, the disk portions where thermal desorption is expected to rule is in turn determined by the binding energies (BEs) of the species to grains. Different BEs imply different temperatures of the dust which can inject iced molecules into the gas-phase (e.g., Penteado et al. 2017).

A recent blooming of projects focused on protoplanetary disks, mainly with ALMA[2], led to the detection of several molecules from CO isotopologues to complex species such as t-HCOOH, CH$_3$OH, and CH$_3$CN (see Öberg et al. 2013, 2015a,b; Öberg & Bergin 2016; Guilloteau et al. 2016; Favre et al. 2015, 2018, 2019; Fedele et al. 2017; Semenov et al. 2018; Podio et al. 2019, 2020a,b; Garufi et al. 2020). The ALMA images allowed the authors to compare the gas and dust distribution, starting the first steps of physical-chemical modelling. A breakthrough result provided by ALMA, through (sub-)mm array observations of young stellar objects, is that planets start to form already during the protostellar phases hence before the classical protoplanetary stage with an age of at least 1 Myr. This is indirectly indicated by the presence of rings, gaps, and spirals in disks with ages less than 1 Myr (see e.g., Sheehan & Eisner 2017; Fedele et al. 2018; Andrews et al. 2018). These substructures have been observed also using molecules, driving studies to sample the molecular components of disks. This is the goal of the ALMA-DOT project (ALMA chemical survey of Disk-Outflow sources in Taurus), which targets Class I or early Class II disks to obtain their chemical characterization.

1.1. The S-bearing molecules

Chemistry of S-bearing species is not well understood. In dense gas, which is involved in the star forming process, sulphur is severely depleted (e.g. Wakelam et al. 2004; Phuong et al. 2018; Tieftrunk et al. 1994; Laas & Caselli 2019; van 't Hoff et al. 2020), by at least two orders of magnitude with respect to the Solar System value [S]/[H] = 1.8×10^{-5} (Anders & Grevesse 1989). The main S-carrier species on dust grains, however, are still unknown. For years, H$_2$S has been postulated to be the solution, but so far it has been never directly detected on interstellar ices (Boogert et al. 2015). Alternative solutions have been proposed in light of studies focused on protostellar shocks, where dust is sputtered: S, OCS, or H$_2$CS (e.g. Wakelam et al. 2004; Codella et al. 2005; Podio et al. 2014; Holdship et al. 2016), but, again, no detection on ices has been reported (Boogert et al. 2015). What about the inventory of S-molecules in protoplanetary disks? Only four species have been detected, often by single-dish: CS, SO, H$_2$S, and H$_2$CS. More specifically, multi-line CS emission has been observed towards $\geq$ 10 disks (e.g. Dutrey et al. 1997, 2017; Fuente et al. 2010; Guilloteau et al. 2013, 2016; Teague et al. 2018; Phuong et al. 2018; Semenov et al. 2018; Le Gal et al. 2019; Garufi et al. 2020; Podio et al. 2020a). SO emission has been detected in fewer disks, part of them still associated with accretion, as e.g. TMC-1A (e.g. Fuente et al. 2010; Guilloteau et al. 2013, 2016; Sakai et al. 2016; Pacheco-Vázquez et al. 2016; Teague et al. 2018; Booth et al. 2018). On the other hand, only very recently H$_2$S and H$_2$CS have been detected and imaged towards a couple of disks. Namely, H$_2$S has been imaged towards GG Tau A (Phuong et al. 2018), while H$_2$CS has been observed with ALMA towards MWC480, and, tentatively, LkCa 15 (Le Gal et al. 2019; Loomis et al.

2020). Further observations of the S-species supposed to be the main S-carrier on dust grains are required.

In this context, the goal of the present project is twofold: (1) to map the H$_2$CS (thioformaldehyde) spatial distribution in protoplanetary disks in an intermediate phase between Class I and Class II, and (2) to derive the binding energies of H$_2$CS using quantum mechanical calculations for an extended crystalline ice. We focus on H$_2$CS in the effort to identify S-bearing species able to trace protoplanetary disks. The article is organized as follows: we first present the observations and data reduction process (Sect. 2), then we report the observational results (Sect. 3), and present the method and the assumptions used to derive BEs (Sect. 4). In Sect. 5, the results will be discussed by comparing the H$_2$CS maps with (i) those of other molecular species as well as with (ii) the spatial distributions expected in case the thermal desorption process (driven by the BE values) is the main mechanism leading to H$_2$CS in the gas-phase. Finally, Sect. 6 summarises our work.

2. Observations: sample and data reduction

The sample consists of four Class I and one early Class II (e.g. Andre et al. 2000) well known sources (Guilloteau et al. 2013, 2014): DG Tau, DG Tau B, HL Tau, IRAS 04302+2247, and Haro 6–13 (aka V 806 Tau). The sources are observed in the context of the ALMA-DOT project (ALMA chemical survey of Disk-Outflow sources in the Taurus star forming region, Podio et al. 2019, 2020a; Garufi et al. 2020), which targets sources: (i) still embedded in a dense envelope, (ii) driving an atomic jet, and a molecular outflow. The sources are chemically rich as revealed by IRAM-30m observations detecting CO isotopologues, H$_2$CO, and CN (plus SO for all but Haro 6–13) (Guilloteau et al. 2013).

This work is based on ALMA Cycle 4 observations of DG Tau and DG Tau B and Cycle 6 observations of HL Tau, IRAS 04302+2247, and Haro 6-13 (projects 2016.1.00846.S and 2018.1.01037.S, PI: L. Podio). The DG Tau and DG Tau B observations were described by Podio et al. (2019), and Garufi et al. (2020), respectively. All Band 6 observations were taken in an extended array configuration with baselines ranging from 15 m to 1.4 km or from 17 m to 3.7 km. The frequency interval covered by the continuum spectral window included the o–H$_2$CS($7_{1,6} - 6_{1,5}$) line emitting at 244048.5 MHz, characterised[3] by $E_{up} = 60$ K, and $S\mu^2 = 56$ D^2. A standard data reduction was performed with CASA pipeline version 4.7.2. Self-calibration was performed on the continuum emission and then applied to the continuum-subtracted line datacube. The r.m.s. for continuum images are about 68 μJy (HL Tau) and 40 μJy (IRAS 04302+2247). The line spectral cube was produced through TCLEAN. We used robust weighting in order to maximise the spatial resolution, and set a channel width of 1.2 km s^{-1}. The r.m.s. per each channel is about 0.8 mJy beam^{-1}. The synthesized beam (HPBW) is $\sim 0\rlap{.}''3 \times 0\rlap{.}''3$.

3. Observational results

3.1. Continuum and H$_2$CS spatial distributions

Out of the 5 observed targets, we detected o–H$_2$CS($7_{1,6} - 6_{1,5}$) emission towards 2 disks, namely HL Tau and IRAS 04302+2247 (herafter IRAS04302). For DG Tau, DG Tau B, and Haro 6–13 upper limits on H$_2$CS emission will be reported

---

[2] Atacama Large Millimeter Array: https://www.almaobservatory.org

[3] The spectral parameters (Maeda et al. 2008) are taken from the Cologne Database for Molecular Spectroscopy (Müller et al. 2005).

in the next sections. As a reference to analyse molecular emission, Figure 1 (upper panels) reports the dust continuum emission. The well known HL Tau disk (d = 147 pc; Galli et al. 2018), with an inclination angle i of 47° (e.g ALMA Partnership et al. 2015; Carrasco-González et al. 2019), is well traced, showing a radius of $\sim$ 150 au. The dust continuum at 227 GHz peaks (118 mJy beam^{-1}) at α(J2000) = 04^h 31^m 38^{s}44, δ(J2000) = +18° 13′ 57″65. On the other hand, the IRAS04302 disk Guilloteau et al. (2013); Podio et al. (2020a), located at d = 161 pc (Galli et al. 2019), is more extended ($\sim$ 350 au), and is associated with an almost edge-on geometry, $i \sim$ 90° (Wolf et al. 2003). The coordinates of the continuum peak, 133 mJy beam^{-1}, are α(J2000) = 04^h 33^m 16^{s}47, δ(J2000) = +22° 53′ 20″36.

Figure 1 (Middle) reports also the intensity integrated maps (moment 0) of the o–H$_2$CS($7_{1,6} - 6_{1,5}$) emission as observed towards HL Tau and IRAS04302, thus providing for the first time the thioformaldeyde radial (HL Tau) and vertical (IRAS04302) distributions. All the channels showing emission of at least 3σ (see Sect. 2) have been used, namely: 3–11 km s^{-1} (HL Tau) and 2–10 km s^{-1} (IRAS04302). The Signal-to-Noise (S/N) of the velocity integrated emission is, in both sources, larger than 8. For HL Tau, the image clearly shows an H$_2$CS ring around a central dip. The outer radius is about 140 pc, while the dip is confined in the inner $\sim$ 35 au. For IRAS04302, the picture as provided by the mom 0 map is less clear. Surely, the H$_2$CS emission is confined in the inner 0″7, $\sim$ 115 au. In Sect. 3, we will show how kinematics will lead us to infer the structure of the emitting region.

Finally, Figure 1 (Bottom panels) reports, in colour scale, the HL Tau and IRAS04302 H$_2$CS($7_{1,6} - 6_{1,5}$) spatial distributions of the peak intensity as derived using the moment 8 method[4] to enlight the images. The moment 8 CASA algorithm has been used by collapsing the intensity axis of the ALMA datacube to one pixel and setting the value of that pixel (for R.A. and Dec.) to the maximum value of the spectrum. The moment 8 images definitely confirm what found with the moment 0 maps. In Sect. 5.2, the spatial distribution will be compared with those of other molecular species.

3.2. H$_2$CS kinematics

Figures 2 and 3 summarise the kinematics of HL Tau and IRAS04302 provided by: (i) channel maps, (ii) intensity weighted mean velocity (moment 1) maps, and (iii) H$_2$CS spectra as extracted towards the brightest positions. The H$_2$CS in HL Tau is clearly rotating with the blue- and red-shifted sides located towards SE and NW, respectively. The systemic velocity is $\sim$ +7.0 km s^{-1} (in agreement with ALMA Partnership et al. 2015; Wu et al. 2018). The same rotating gradient has been observed using HCO$^+$ (ALMA Partnership et al. 2015; Yen et al. 2019), C^{18}O (Wu et al. 2018), and ^{13}C^{17}O (Booth & Ilee 2020). Also the emission towards IRAS04302 disk shows a rotation pattern. Its almost edge-on orientation allows us to clearly disentangle the red- (southern) and blue-shifted (northern) lobes. The systemic velocity estimated from the velocity distribution of the bright H$_2$CO line is +5.6 km s^{-1} (Podio et al. 2020a), in good agreement with IRAM 30-m CN, H$_2$CO, CS, and C^{17}O spectra of Guilloteau et al. (2013, 2016). The rotation pattern has been imaged also by Podio et al. (2020a), who found, using CO, H$_2$CO, and CS emission, a molecular emission which is vertically stratified (see Sect. 4 for the comparison with H$_2$CS).

The H$_2$CS channel maps show that the emission shifted by less than 2 km s^{-1} is emitted from the inner 0″5 region, whereas at larger velocities we detect emission up to 1″2 from the protostar. This suggests that larger projected velocities (in particular the blue-shifted velocity) have a larger projected positional offset from the protostar. In other words, the present dataset suggests that V $\propto$ R. This is the standard signature of a rotating ring with an inner dip, and not a filled disk, where we would have an opposite trend, with V $\propto$ R^{-2}. Very recently, Oya & Yamamoto (2020) reported the detection of H$_2$CS in the IRAS16293 A protostellar disk (see also van 't Hoff et al. 2020). In addition, the present findings well resamble what found in the archetypical protostellar disk HH212, also close to be edge-on as IRAS04302 (e.g. Lee et al. 2019, and references therein). Also in this case, a chemical enrichment in the gas phase associated with rotating rings is revealed by the V $\propto$ R kinematical feature (see e.g. the recent review by Codella et al. 2019).

3.3. H$_2$CS column densities and abundances

Assuming (i) Local Thermodynamic Equilibrium (LTE), and (ii) optically thin emission, the column densities of the H$_2$CS are derived. The first assumption is well justified as the H$_2$ gas density in the molecular layers is larger than 10^7 cm^{-3} (see e.g. Walsh et al. 2014; Le Gal et al. 2019), i.e. well above the critical density of the considered o-H$_2$CS($7_{1,6}-6_{1,5}$) line ($n_{cr} \sim$ a few 10^4 cm^{-3} in the 20–150 K range[5]. The second assumption is justified as models indicate an abundance (with respect to H) of H$_2$CS lower than 10^{-10} (Le Gal et al. 2019; Loomis et al. 2020).

In HL Tau the observed emitting area is 1.35 arcsec^2 (from the moment 0 map) the flux is 148 mJy km s^{-1} (2.6 K km s^{-1}). Le Gal et al. (2019) estimated an H$_2$CS rotational temperature between 20 K and 80 K in the MWC 480 disk. We conservatively adopted a temperature between 20 K and 150 K. An ortho-to-para ratio of 3, i.e. the statistical value, has been assumed (as done by Le Gal et al. 2019). The total H$_2$CS column density (averaged on the emitting area) N_{H_2CS} turns out to be 0.9–1.4 $\times$ 10^{14} cm^{-2}. For IRAS04302 the emitting area is smaller with respect to HL Tau, 0.72 arcsec^2 and the flux is $\simeq$ 78 mJy km s^{-1} (2.5 K km s^{-1}). The column density N_{H_2CS} is, similarly to HL Tau, $\simeq$ 10^{14} cm^{-2}. These values can be also considered as an a-posteriori check that the observed H$_2$CS emission is optically thin. Indeed, by assuming kinetic temperatures larger than 20 K and densities larger than 10^7 cm^{-3}, the Large Velocity Gradient approach confirms that column densities around 10^{14} cm^{-2} implies for the o-H$_2$CS($7_{1,6}-6_{1,5}$) line an opacity of $\leq$ 0.1. These column density estimates are larger by a factor 30 with respect to the ones measured by Le Gal et al. (2019) and Loomis et al. (2020) towards the massive disk MWC 480 (3 $\times$ 10^{12} cm^{-2}). However, as reported by the authors, their spatial resolution is not high enough to evaluate the presence of a central dip, which could cause an underestimate the H$_2$CS column density.

For HL Tau a further step can be done given that Booth & Ilee (2020) published an ALMA map of the ^{13}C^{17}O(3–2) emission at a similar angular scale as our H$_2$CS maps. The ^{13}C^{17}O spatial distributions well agrees with that of H$_2$CS. The emission is considered optically thin, given that its abundance ratio with respect to ^{12}C^{16}O is 8.3 $\times$ 10^{-6} (Milam et al. 2005). Taking the ^{13}C^{17}O flux density of 10-20 mJy beam^{-1} km s^{-1}, and an excitation temperature, as for H$_2$CS, in the 20-150 K range, we derive $N_{CO} \simeq$ 5–10 $\times$ 10^{23} cm^{-2}. Using [CO]/[H] = 5 $\times$ 10^{-5}, the

---

[4] https://casa.nrao.edu/Release3.4.0/docs/UserMan/UserManse41.html

[5] Using scaled H$_2$CO collisional rates from Wiesenfeld & Faure (2013), see Schöier et al. (2005).

H_2CS abundance (with respect to H) results to be $X(H_2CS) \simeq 10^{-14}$. The comparison with the H_2CS abundances predicted by disk chemistry is challenging, given this is dramatically depending on the initial composition of the S-species, which can vary by orders of magnitude (see e.g Fedele & Favre 2020). Vice versa, the present measured H_2CS abundances will be hopefully used in future chemical models to constrain their initial conditions.

Finally, the upper limits on the H_2CS column densities in DG Tau, DG Tau B, and Haro 6-13, derived taking the 5σ level of the moment 0 maps, and using all the assumptions as above, are: $N_{H_2CS} \leq 2 \times 10^{13}$ cm^{-2} (DG Tau B), and $N_{H_2CS} \leq 4 \times 10^{13}$ cm^{-2} (DG Tau and Haro 6-13).

4. Binding energies: ice modelling and computational methods

We computed the H_2CS and CS BEs, adopting for the bulk ice a proton-ordered (P-ice) crystalline model (Casassa et al. 1997). The ice surface where the adsorption takes place was simulated by a finite slab model of the (010) surface cut out from the bulk P-ice crystal, as recently proposed by Ferrero et al. (2020) to predict the BEs of a set of 21 molecules using the periodic *ab initio* program CRYSTAL17 (Dovesi et al. 2018). CRYSTAL17 adopts localised (Gaussian) basis functions which allow to simulate the surfaces as a true 2D systems, without including fake replicas of the slab separated by artificial voids. The surface slab model is thick enough (number of water layers) to ensure a converged surface energy (energy penalty to cut the surface from the bulk ice). The choice of a crystalline ice model is against the overwhelming evidence that ice in the interstellar environment is of amorphous nature (AWS). There are two main reasons that hinder the adoption of AWS phase at the modeling level: i) the experimental atomistic structure of the AWS is unknown; ii) AWS model should be based on very large unit cell to mimic the disorder nature of the ice. Point i) means that the model cannot be derived from experimental evidence and therefore any model is somehow arbitrary. Point ii) implies that very expensive calculations are needed to cope with the large unit cells. In the following, we proposed a simplified strategy to derive the values of the BEs for the H_2CS and CS molecules as adsorbed on AWS, without actually run the needed expensive calculations, but taking profit of the results by Ferrero et al. (2020) on the analogous CO and H_2CO molecules, in which both crystalline and AWS models were studied.

First, we set up the starting locations of H_2CS and CS molecules at the ice surface using the optimized positions of the analogous CO and H_2CO molecules after Ferrero et al. (2020) and then fully optimizing the structures. We choose the HF-3c method, which combines the Hartree-Fock Hamiltonian with the minimal basis set MINI-1 (Tatewaki & Huzinaga 1980) supplemented by three *a posteriori* corrections for: (i) the basis set superposition error (BSSE), arising when localized Gaussian functions are used to expand the basis set (Jansen & Ros 1969; Liu & McLean 1973); (ii) the dispersive interactions; (iii) short-ranged deficiencies due to the adopted minimal basis set (Sure & Grimme 2013). The resulting optimized unit cell of the ice (010) surface is shown in Figure 4, together with the mapping of the electrostatic potential (ESP) computed at HF-3c level of theory. The ESP reveals the oxygen rich (red color, ESP < 0) and proton rich (blue color, ESP > 0) regions, acting, respectively, as a H-bond acceptor/donor with respect to specific adsorbates.

In order to get accurate BEs, the HF-3c structures were used to compute single point energy evaluation at B3LYP-D3(BJ)

level of theory (Becke 1993). Dispersion interaction is included through the D3 correction, with the Becke-Johnson damping scheme (Grimme et al. 2010). The Ahlrichs' triple-zeta quality VTZ basis set, supplemented with a double set of polarization functions (Schäfer et al. 1992) was adopted to define the final B3LYP-D3(BJ)/A-VTZ*//HF-3c model chemistry. BEs were also corrected for BSSE.

For H_2CS, the most stable structure shows a symmetric involvement of the CH_2S molecule with the ice surface, in which the C-H bonds act as weak H-donors toward the surface oxygen atoms, while the S atom as a H-bond acceptor at the dangling surface OH groups. For CS, the adsorption occurs through the C-end with a very long H-bond with the dangling ice OH group. Any attempt to engage the CS molecule through the S end of the molecule evolved spontaneously to the C-end one. Obviously, the relatively simple structure of the crystalline P-ice does not allow to explore other configurations than the described ones, at variance with the results for an AWS model which would be expected to provide a many-fold of adsorption sites of different strength. Furthermore, due to the long range order of the water molecules in the crystalline ice, the H-bond interactions will co-operate to enhance the H-bond donor/acceptor character of the surface water molecules, giving very high/low values of the ESP (see Figure 4). This means that the BEs resulting from the crystalline model should be taken as an upper limit, as shown by Ferrero et al. (2020). As anticipated, to remedy the deficiencies of the crystalline ice model we resort to data from the work by Ferrero et al. (2020) for the analog CO and H_2CO molecules (with respect to CS and H_2CS treated here) adsorbed on the AWS model. As expected, they found a rather complex adsorption scenario at AWS, when compared to that occurring at the P-ice surface. For CO, five different adsorption sites have been characterized; for H_2CO, up to eight different adsorption sites were predicted. Obviously, each of these adsorption sites provides different values of the BE and in the limit of very large AWS models, the BE values will obey to a certain distribution. It is clear that a similar painstacking study should be carried out also for CS and H_2CS. Instead, as anticipated, we resort to a simplified scheme to guess the BE values for the AWS, without actually running any calculation.

First, from the data by Ferrero et al. (2020), we worked out two scaling factors (0.859 and 0.775, respectively) connecting the BE of the CO and H_2CO analogs computed for the P-ice to their corresponding averaged BE values for the AWS model. Then by assuming the same scaling factors also for the present CS and H_2CS cases, we scaled the BEs for the crystalline ice to estimate their averaged values on the AWS model. In agreement with the CO and H_2CO cases, also for CS and H_2CS the BE-AWS are smaller than those for the crystalline ice. Table 1 reports, for both H_2CS and CS, the derived BEs on crystalline (H_2CS: 4258 K; CS: 3861 K) and AWS (H_2CS: 3000-4600 K; CS: 2700-4000 K) ice.

5. Discussion

5.1. Comparison with previous BEs measurements

Interstellar molecules are formed either through gas-phase reactions or directly on grain surfaces. Regardless of the formation route, gaseous molecules freeze out into the grain mantles in timescales that depend on the density and temperature of the gas and dust as well as the molecule BE. Thus, in cold and dense regions, as in the outer disk regions and in the layers close to the disk midplane, icy mantles envelope the dust grains. The frozen

Table 1. H$_2$CS and CS BEs (Kelvin) derived for the crystalline (CRY) and amorphous (AWS) ice models. See the text for the procedure adopted to arrive to the BE-AWS values

	BE-CRY	BE-AWS	Das[a]	Wakelam[b]
H$_2$CS	4258	3000–4600	3110	4400
CS	3861	2700–4000	2217	3200

[a] Das et al. (2018); [b] Wakelam et al. (2017).

molecules can then be injected into the gas-phase via three processes (see e.g. Walsh et al. 2014): (i) thermal desorption, (ii) UV-photo and/or CR-induced desorption, and (iii) reactive desorption. The first process occurs inside the so called snow lines, i.e. the location where the dust temperature is high enough to allow the species to sublimate.

Regarding H$_2$CO, its BE has been experimentally measured on amorphous water surface (AWS) through thermal desorption process, e.g. by Noble et al. (2012) to be 3260±60 K, and estimated via theoretical computations on AWS and crystalline ice models by Ferrero et al. (2020), who found zero point corrected BEs (see Sect. 4) in the 3071-6194 K range, for the AWS case, therefore bracketing the experimental value. The BE for the crystalline ice falls at 5187 K, in the higher regime of the AWS range.

Following the described procedure, we found for H$_2$CS BE values of 4258 K and 3000–4600 K for the crystalline and AWS ice models, respectively. For CS, we have slightly lower values: 3861 K (crystalline) and 2700–4000 K (AWS). Table 1 compares our results with the available literature data, all coming from computer simulations. The BE computed by Das et al. (2018), who adopted a tetramer of water molecules to simulate the ice, are in the low end of our computed BEs range, whereas the BE computed by Wakelam et al. (2017), based on one single water and corrected with an empirical factor, lies on the high end of our range.

Based on our new computations of Sect. 4 and using a BE ranging from 3000 to 4600 K, H$_2$CS is expected to thermally sublimate in regions of the disk where the dust temperature exceeds ~50 to ~80 K, respectively. We emphasise that the dispersion in our computed BEs reflects the different possible sites of adsorption of H$_2$CS and it is, therefore, physical and not due to a computational uncertainty (see the discussion in Ferrero et al. 2020). Although we cannot a priori say how many sites with each different BE are populated, we can conservatively assume that H$_2$CS molecules should remain frozen in regions of the disk with dust temperatures lower than 50–80 K. The fact that H$_2$CS emission up to outer radii of ∼ 140 au (HL Tau) and ∼ 115 au (IRAS 04302) suggests that non thermal processes are likely responsible for the presence of H$_2$CS in the gas in those disk regions.

5.2. Comparison between H$_2$CS, CS, and H$_2$CO

The formation routes of H$_2$CS have been recently summarised by Le Gal et al. (2019), who used the the gas-grain chemical model *Nautilus* (Wakelam et al. 2016) supported by the gas chemical dataset *KIDA* (Wakelam et al. 2015), and by Fedele & Favre (2020), who adopted the thermo-chemical model *DALI* (Bruderer et al. 2012), coupled with the chemical network *UMIST* (Woodall et al. 2007). Generally, H$_2$CS is mainly (99%) formed in gas-phase via neutral–neutral reaction of atomic S with CH$_3$. On the other hand, CS in disks is also thought to be mainly formed in gas-phase, through reactions starting with

small hydrocarbons interacting with S$^+$ (in upper disk layers) or S (in inner slabs). Finally, H$_2$CO can be formed on grains due to hydrogenation processes as well and in gas-phase by oxygen reacting with CH$_3$, in a analogous way of S + CH$_3$ → H$_2$CS (see e.g. Fedele & Favre 2020, and references therein).

For the IRAS04302 disk, the H$_2$CS vertical intensity profile can be compared with those of CS and formaldehyde (H$_2$CO), by Podio et al. (2020a). For such a purpose, we averaged the emission radially over 3 pixels (0.′′18, corresponding to ∼ 29 au) around the selected radius. Figure 5 reports the comparison obtained at 60 au and 115 au from the protostar. Note that the H$_2$CS intensity has been multiplied by the factor reported in the labels in order to better compare with those of o-H$_2$CO and CS. The vertical distribution of H$_2$CS (black) shows an asymmetry with respect to the disk midplane (i.e. $z = 0$), with the emission from the eastern disk side being brighter than in the western side by a factor 1.8 at 60 au radial distance and a factor 1.5 at 115 au. The same asymmetry in the vertical distribution is observed in the H$_2$CO (blue) and CS (red) emission, and all the three species peak at a disk height, z of about 50 au. This suggests that at our resolution the emission from H$_2$CS, H$_2$CO, and CS originate from the same disk layer. As discussed by Podio et al. 2020, the bulk of the H$_2$CO and CS emission originate from the disk molecular layer where molecules are either released from dust grains and/or formed in gas-phase. Given that H$_2$CS is cospatial with H$_2$CO and CS and that all the three molecules can be efficiently formed in gas-phase using small hydrocarbons (e.g. CH$_3$), we suggest that H$_2$CS may form in similar way.

The comparison between the moment 0 distributions of H$_2$CS with those of H$_2$CO (Podio et al. 2020a) is also instructive (see Fig. 6), showing a slightly different radial distribution of H$_2$CO and H$_2$CS. The H$_2$CO (and CS) emissions extend radially out to ∼ 480 au and peak at ∼ 120 au, while the H$_2$CS emission is radially confined in the inner 115 au with a peak at ∼ 70 au. The radial distribution of H$_2$CS suggests that the o–H$_2$CS($7_{1,6}-6_{1,5}$) line probes an inner portion of the IRAS04302 disk, possibly due a higher E_{up}, 60 K, with respect to those of the o–H$_2$CO($3_{1,2}-2_{1,1}$) and CS(5–4), 33–35 K. Only further observations of a species using different excitation lines will shed light on this hypothesis.

6. Conclusions

We presented the first images of the radial (HL Tau) and vertical (IRAS04302) spatial distribution of the o-H$_2$CS emission as observed towards Class I protoplanetary disks using ALMA on a Solar System scale. The observations have been performed in in the context of the ALMA chemical survey of Disk-Outflow sources in the Taurus star forming region (ALMA-DOT). H$_2$CS is confined in a rotating ring with an inner dip towards the protostar: the outer radii are 140 au (HL Tau) and 115 au (IRAS04302). The edge-on geometry of IRAS 04302 allows us to reveal that H$_2$CS emission peaks, (at $r = 60$–115 au), at $z = \pm 50$ au from the equatorial plane. Assuming LTE conditions, the column densities are ∼ 10^{14} cm^{-2}. For HL Tau, we derived, for the first time, the [H$_2$CS]/[H] abundance in a protoplanetary disk ($\simeq 10^{-14}$). The o–H$_2$CS($7_{1,6}-6_{1,5}$) line emits where the emission of CS(5–4) and o–H$_2$CO($3_{1,2}-2_{1,1}$) is brighter (Podio et al. 2020a), i.e. the so-called warm molecular layer. H$_2$CS emission peaks closer to the protostar with respect to H$_2$CO and CS, possibly due to the higher energy of the upper level (60 K) of the observed transition with respect to those of H$_2$CO and CS (33-35 K), which requires higher gas temperature hence favouring the emission from the inner disk regions.

The present work also provides the H$_2$CS and CS BEs as computed for the first time for an extended crystalline ice (4258 K, H$_2$CS, and 3861 K, CS) and estimated for an AWS model using recipes from previous work (Ferrero et al. 2020) to be in the 3000-4600 K and 2700-4000 K range. In turn, for $\sim 1\ L_\odot$ protostars, this implies that radially thermal desorption rules in an inner region, while vertically only a thin upper layer is hot enough (see e.g. Walsh et al. 2014; Le Gal et al. 2019). To conclude, the observed H$_2$CS, more precisely that detected at radii up to more than 100 au, is released into the gas likely due to non-thermal processes (photo-/CR- and/or reactive-desorption).

References

ALMA Partnership, Brogan, C. L., Pérez, L. M., et al. 2015, ApJ, 808, L3

Anders, E. & Grevesse, N. 1989, Geochim. Cosmochim. Acta, 53, 197

Andre, P., Ward-Thompson, D., & Barsony, M. 2000, From Prestellar Cores to Protostars: the Initial Conditions of Star Formation

Andrews, S. M., Huang, J., Pérez, L. M., et al. 2018, ApJ, 869, L41

Becke, A. D. 1993, J. Chem. Phys., 98, 1372

Belloche, A., Maury, A. J., Maret, S., et al. 2020, A&A, 635, A198

Boogert, A. C. A., Gerakines, P. A., & Whittet, D. C. B. 2015, Observations of the icy universe.

Booth, A. S. & Ilee, J. D. 2020, MNRAS, 493, L108

Booth, A. S., Walsh, C., Kama, M., et al. 2018, A&A, 611, A16

Bruderer, S., van Dishoeck, E. F., Doty, S. D., & Herczeg, G. J. 2012, A&A, 541, A91

Carrasco-González, C., Sierra, A., Flock, M., et al. 2019, ApJ, 883, 71

Casassa, S., Ugliengo, P., & Pisani, C. 1997, The Journal of Chemical Physics, 106, 8030

Caselli, P. & Ceccarelli, C. 2012, A&A Rev., 20, 56

Ceccarelli, C., Caselli, P., Fontani, F., et al. 2017, ApJ, 850, 176

Ceccarelli, C., Caselli, P., Herbst, E., Tielens, A. G. G. M., & Caux, E. 2007, in Protostars and Planets V, ed. B. Reipurth, D. Jewitt, & K. Keil, 47

Codella, C., Bachiller, R., Benedettini, M., et al. 2005, MNRAS, 361, 244

Codella, C., Ceccarelli, C., Lee, C.-F., et al. 2019, ACS Earth and Space Chemistry, 3, 2110

Das, A., Sil, M., Gorai, P., Chakrabarti, S. i. K., & Loison, J. C. 2018, ApJS, 237, 9

Dovesi, R., Orlando, R., Erba, A., et al. 2018, Wiley Interdiscip Rev Comput Mol Sci, 176

Dutrey, A., Guilloteau, S., & Guelin, M. 1997, A&A, 317, L55

Dutrey, A., Guilloteau, S., Piétu, V., et al. 2017, A&A, 607, A130

Favre, C., Bergin, E. A., Cleeves, L. I., et al. 2015, ApJ, 802, L23

Favre, C., Fedele, D., Maud, L., et al. 2019, ApJ, 871, 107

Favre, C., Fedele, D., Semenov, D., et al. 2018, ApJ, 862, L2

Fedele, D., Carney, M., Hogerheijde, M. R., et al. 2017, A&A, 600, A72

Fedele, D. & Favre, C. 2020, A&A, 638, A110

Fedele, D., Tazzari, M., Booth, R., et al. 2018, A&A, 610, A24

Ferrero, S., Zamirri, R., Ceccarelli, C., et al. 2020, ApJ, in press

Fuente, A., Cernicharo, J., Agúndez, M., et al. 2010, A&A, 524, A19

Galli, P. A. B., Loinard, L., Bouy, H., et al. 2019, A&A, 630, A137

Galli, P. A. B., Loinard, L., Ortiz-Léon, G. N., et al. 2018, ApJ, 859, 33

Garufi, A., Podio, L., Codella, C., et al. 2020, arXiv e-prints, arXiv:2002.10195

Grimme, S., Antony, J., Ehrlich, S., & Krieg, H. 2010, J. Chem. Phys., 132, 154104

Guilloteau, S., Di Folco, E., Dutrey, A., et al. 2013, A&A, 549, A92

Guilloteau, S., Reboussin, L., Dutrey, A., et al. 2016, A&A, 592, A124

Guilloteau, S., Simon, M., Piétu, V., et al. 2014, A&A, 567, A117

Herbst, E. & van Dishoeck, E. F. 2009, ARA&A, 47, 427

Holdship, J., Viti, S., Jimenez-Serra, I., et al. 2016, MNRAS, 463, 802

Jansen, H. & Ros, P. 1969, Chemical Physics Letters, 3, 140

Jørgensen, J. K., van der Wiel, M. H. D., Coutens, A., et al. 2016, A&A, 595, A117

Laas, J. C. & Caselli, P. 2019, Modeling sulfur depletion in interstellar clouds

Le Gal, R., Öberg, K. I., Loomis, R. A., Pegues, J., & Bergner, J. B. 2019, ApJ, 876, 72

Lee, C.-F., Li, Z.-Y., & Turner, N. J. 2019, Nature Astronomy, 466

Lefloch, B., Bachiller, R., Ceccarelli, C., et al. 2018, MNRAS, 477, 4792

Liu, B. & McLean, A. D. 1973, The Journal of Chemical Physics, 59, 4557

Loomis, R. A., Cleeves, L. I., Öberg, K. I., Guzman, V. V., & Andrews, S. M. 2015, ApJ, 809, L25

Loomis, R. A., Öberg, K. I., Andrews, S. M., et al. 2020, ApJ, 893, 101

Maeda, A., Medvedev, I. R., Winnewisser, M., et al. 2008, ApJS, 176, 543

Milam, S. N., Savage, C., Brewster, M. A., Ziurys, L. M., & Wyckoff, S. 2005, ApJ, 634, 1126

Müller, H. S. P., Schlöder, F., Stutzki, J., & Winnewisser, G. 2005, Journal of Molecular Structure, 742, 215

Noble, J. A., Theule, P., Mispelaer, F., et al. 2012, A&A, 543, A5

Öberg, K. I. & Bergin, E. A. 2016, ApJ, 831, L19

Öberg, K. I., Boamah, M. D., Fayolle, E. C., et al. 2013, ApJ, 771, 95

Öberg, K. I., Furuya, K., Loomis, R., et al. 2015a, ApJ, 810, 112

Öberg, K. I., Guzmán, V. V., Furuya, K., et al. 2015b, Nature, 520, 198

Oya, Y. & Yamamoto, S. 2020, arXiv e-prints, arXiv:2010.01273

Pacheco-Vázquez, S., Fuente, A., Baruteau, C., et al. 2016, A&A, 589, A60

Penteado, E. M., Walsh, C., & Cuppen, H. M. 2017, ApJ, 844, 71

Phuong, N. T., Chapillon, E., Majumdar, L., et al. 2018, A&A, 616, L5

Podio, L., Bacciotti, F., Fedele, D., et al. 2019, A&A, 623, L6

Podio, L., Garufi, A., Codella, C., et al. 2020a, A&A, 642, L7

Podio, L., Garufi, A., Codella, C., et al. 2020b, arXiv e-prints, arXiv:2011.01081

Podio, L., Lefloch, B., Ceccarelli, C., Codella, C., & Bachiller, R. 2014, A&A, 565, A64

Sakai, N., Oya, Y., López-Sepulcre, A., et al. 2016, ApJ, 820, L34

Schäfer, A., Horn, H., & Ahlrichs, R. 1992, J. Chem. Phys., 97, 2571

Schöier, F. L., van der Tak, F. F. S., van Dishoeck, E. F., & Black, J. H. 2005, A&A, 432, 369

Semenov, D., Favre, C., Fedele, D., et al. 2018, A&A, 617, A28

Semenov, D. & Wiebe, D. 2011, Chemical Evolution of Turbulent Protoplanetary Disks and the Solar Nebula

Sheehan, P. D. & Eisner, J. A. 2017, ApJ, 840, L12

Sure, R. & Grimme, S. 2013, Journal Computational Chemistry, 34, 1672

Tatewaki, H. & Huzinaga, S. 1980, Journal of Computational Chemistry, 1, 205

Teague, R., Henning, T., Guilloteau, S., et al. 2018, ApJ, 864, 133

Tieftrunk, A., Pineau des Forets, G., Schilke, P., & Walmsley, C. M. 1994, A&A, 289, 579

van 't Hoff, M. L. R., van Dishoeck, E. F., Jørgensen, J. K., & Calcutt, H. 2020, A&A, 633, A7

Wakelam, V., Bron, E., Cazaux, S., et al. 2017, Molecular Astrophysics, 9, 1

Wakelam, V., Caselli, P., Ceccarelli, C., Herbst, E., & Castets, A. 2004, A&A, 422, 159

Wakelam, V., Loison, J. C., Herbst, E., et al. 2015, ApJS, 217, 20

Wakelam, V., Ruaud, M., Hersant, F., et al. 2016, A&A, 594, A35

Walsh, C., Loomis, R. A., Öberg, K. I., et al. 2016, ApJ, 823, L10

Walsh, C., Millar, T. J., Nomura, H., et al. 2014, A&A, 563, A33

Wiesenfeld, L. & Faure, A. 2013, MNRAS, 432, 2573

Wolf, S., Padgett, D. L., & Stapelfeldt, K. R. 2003, ApJ, 588, 373

Woodall, J., Agúndez, M., Markwick-Kemper, A. J., & Millar, T. J. 2007, A&A, 466, 1197

Wu, C.-J., Hirano, N., Takakuwa, S., Yen, H.-W., & Aso, Y. 2018, ApJ, 869, 59

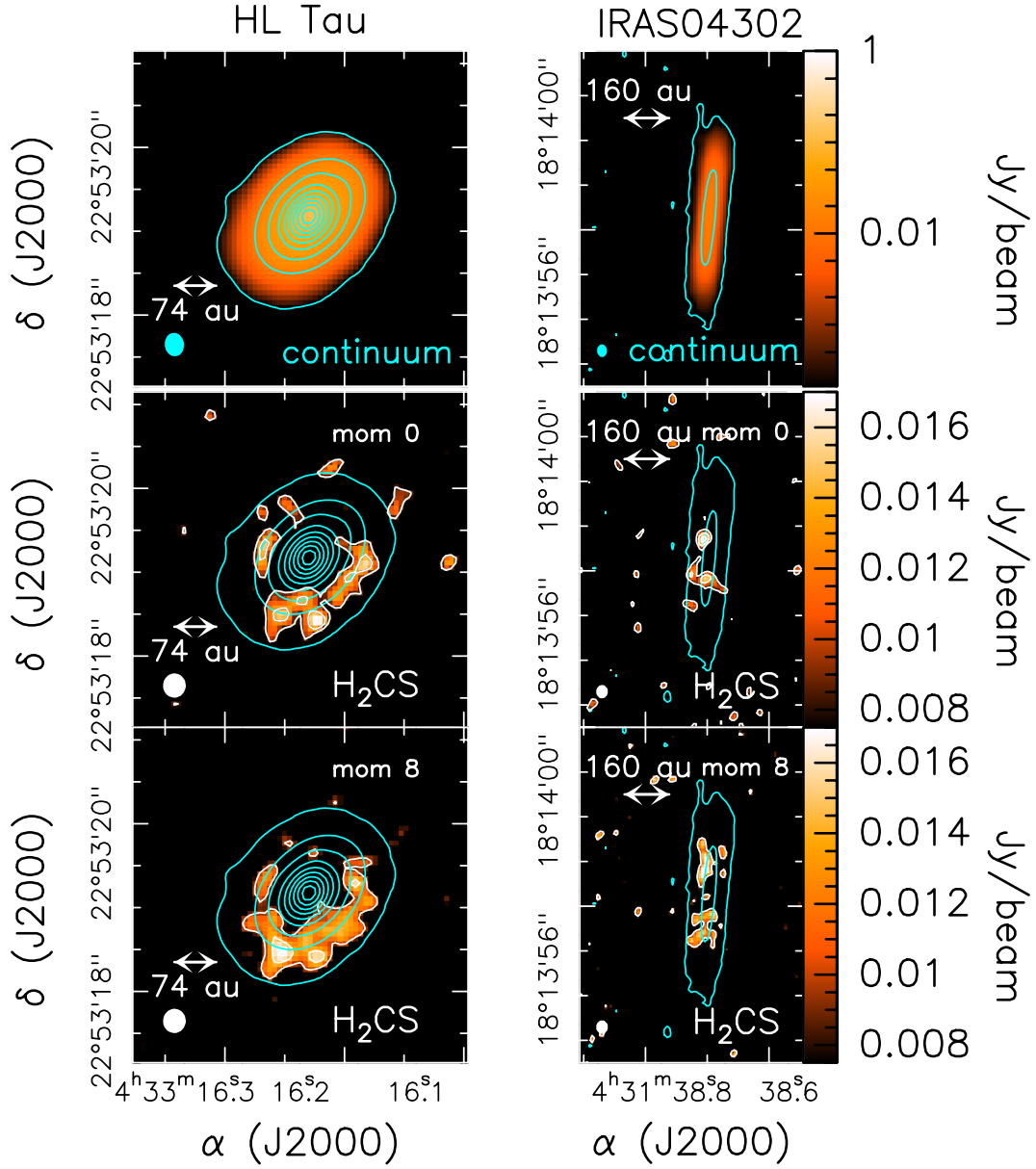Yen, H.-W., Gu, P.-G., Hirano, N., et al. 2019, ApJ, 880, 69

Fig. 1. *Upper panels:* Map (cyan contours and colour scale) of the 1.3mm dust continuum distribution for HL Tau (Left) and IRAS 04302+2247 (Right) disks. First contours and steps are 3σ (200 μJy beam^{-1}, HL Tau; 115 μJy beam^{-1}, IRAS 04302+2247), and 200σ, respectively. The ellipse in the bottom left corner shows the ALMA synthesized beam (HPBW): 0''28 × 0''25 (PA = −7°), for HL Tau, and 0''28 × 0''22 (PA = −3°), for IRAS 04302+2247. *Middle panels:* Spatial distribution (moment 0) maps (white contours and colour scale) of the o–H$_2$CS($7_{1,6}$–$6_{1,5}$) line based on the velocity integrated emission (3–11 km s^{-1}, HL Tau, 2–10 km s^{-1}, IRAS 04302+2247), overlaid on the continuum maps (cyan contours). First contours and steps are 5σ (7.5 mJy beam^{-1} km s^{-1}, HL Tau, and 12.5 mJy beam^{-1} km s^{-1}, IRAS04302), and 3σ, respectively. The ellipse shows the synthesized beam (HPBW): 0''29 × 0''27 (PA = 2°), for HL Tau, and 0''30 × 0''26 (PA = 2°), for IRAS 04302+2247. *Lower panels:* Moment 8 maps (white contours and colour scale) of the H$_2$CS($7_{1,6}$–$6_{1,5}$) based on the same velocity integrated emission used for the moment 0 maps, overlaid on the continuum maps (cyan contours). First contours and steps are 5σ (3 mJy beam^{-1} km s^{-1}), and 3σ, respectively.
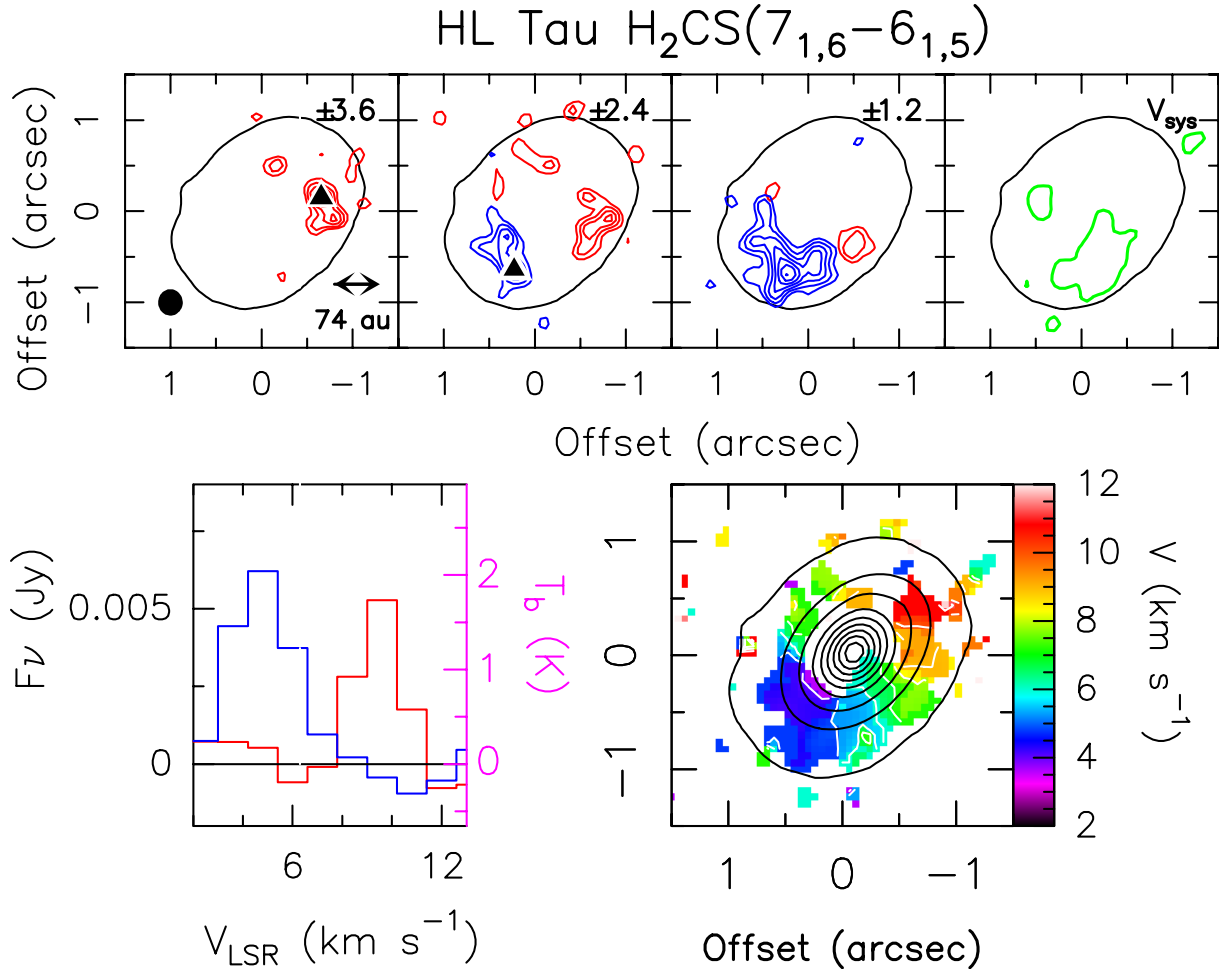
Fig. 2. *Upper:* Channel maps of the o–$H_2CS(7_{1,6}-6_{1,5})$ blue- and red-shifted emission in the HL Tau disk. Each panel shows the emission integrated over a velocity interval of 1.2 km s^{-1} shifted with respect to the systemic velocity ($\sim$ +7 km s^{-1}, green) by the value given in the upper-right corner. We report, in black, the 3σ contour of the continuum emission (Figs. 1, A.1). The black triangles indicate where spectra have been extracted. The ellipse shows the synthesized beam (HPBW): 0.''29 × 0.''27 (PA = 2°). First contours and steps correspond to 3σ (2.1 mJy beam^{-1}) and 1σ, respectively. Offsets are derived with respect to the continuum peak (Sect. A). *Bottom Left:* o–$H_2CS(7_1,6-6_1,5)$ spectra in flux and brightness temperature scales (T_b/F_ν = 328.593) extracted in the positions marked with a red or blue triangle in the Upper panels. *Bottom Right:* First-moment map in colour scale.
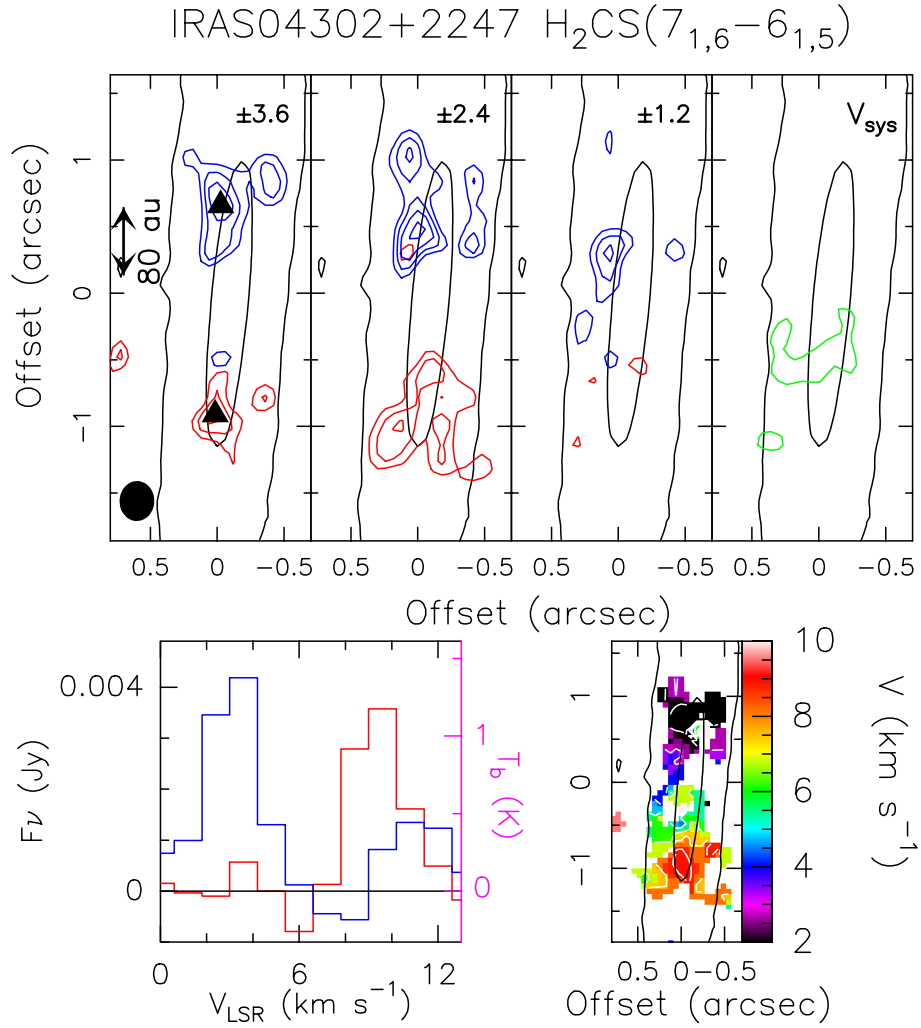
Fig. 3. *Upper:* Channel maps of the o–H₂CS($7_{1,6}$–$6_{1,5}$) blue- and red-shifted emission in the IRAS 04302+2247 disk. Each panel shows the emission integrated over a velocity interval of 1.2 km s^{-1} shifted with respect to the systemic velocity (∼ +5.6 km s^{-1} Podio et al. 2020a, green) by the value given in the upper-right corner. We report,in black, the 3σ contour of the continuum emission (Figs. 1, A.1). The black triangles indicate where spectra have been extracted. The ellipse shows the synthesized beam (HPBW): 0″.30 × 0″.26 (PA = 2°). First contours and steps correspond to 3σ (2.1 mJy beam^{-1}) and 1σ, respectively. Offsets are derived with respect to the continuum peak (Sect. A). *Bottom Left:* o–H₂CS($7_{1,6}$–$6_{1,5}$) spectra in flux and brightness temperature scales (T_{b}/F_{ν} = 328.593) extracted in the positions marked with a red or blue triangle in the Upper panels. *Bottom Right:* First-moment map in colour scale.
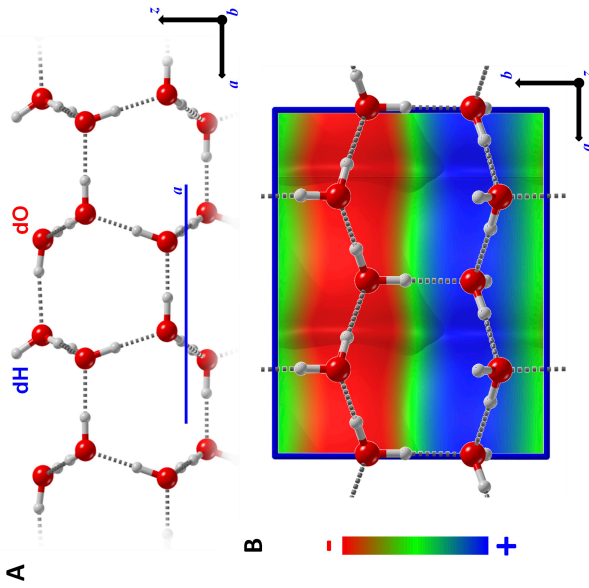
Fig. 4. HF-3c optimized P-ice slab model. The adsorption crystallographic plane is the Miller (010) one. *A Panel:* Side view along the *b* lattice vector. *B Panel:* Top view of the 2×1 supercell ($|a| = 9.065\,\text{Å}$ and $|b| = 7.154\,\text{Å}$) along with its ESP map. Colour code: +0.02 atomic unit (blue, positive), 0.00 atomic unit (green, neutral) and –0.02 atomic unit (red, negative).
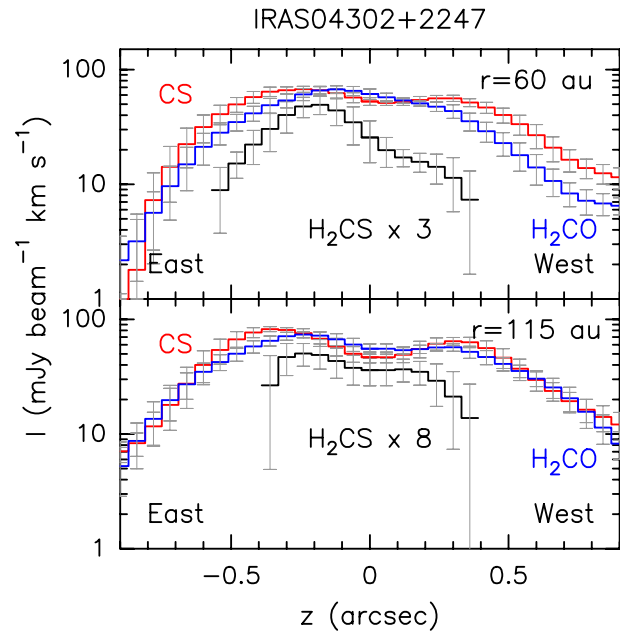
Fig. 5. Vertical intensity profile z of H_2CS (black) compared with those of $CS(5–4)$ (red) and $o\text{-}H_2CO(3_{1,2} - 2_{1,1})$ (blue), from Podio et al. (2020a). Only fluxes above 3σ confidence are shown. The H_2CS intensity has been scaled in order to better compare its profile with those of $o\text{-}H_2CO$ and CS. The inner $1''8$ region is shown, with the positive (negative) values sampling the eastern (western) side. The angular resolution is $0''25$ (40 au). The profiles obtained at ~ 60 au (Upper panel) and 115 au (Lower panel) from the protostar.
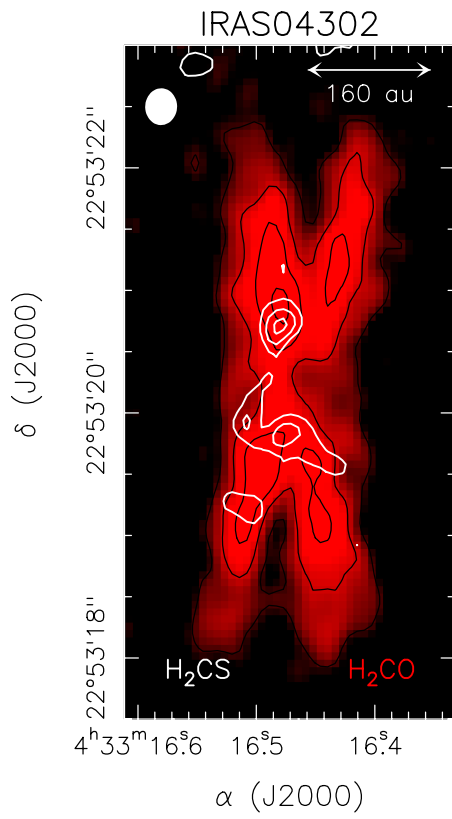
Fig. 6. Spatial distribution (moment 0) maps (white contours) of the o–H$_2$CS($7_{1,6}$–$6_{1,5}$) line (see Fig. 1), overlaid on the o-H$_2$CO($3_{1,2} - 2_{1,1}$) reported by Podio et al. (2020a), in black contours and red scale. Symbols are as in Figure 1.